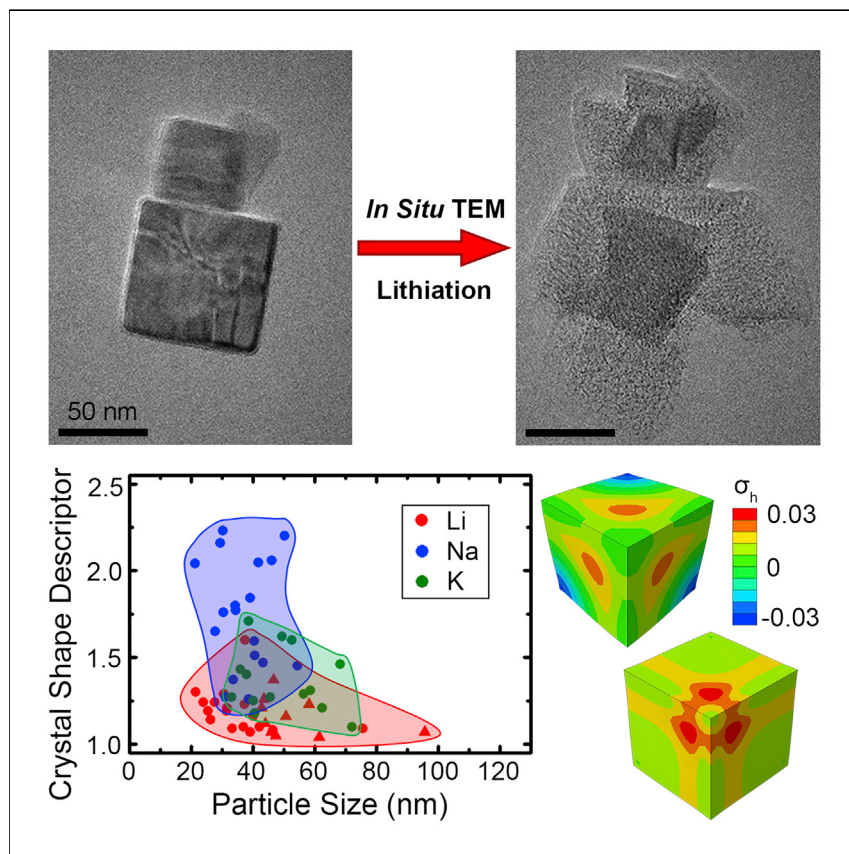


## Article

# Avoiding Fracture in a Conversion Battery Material through Reaction with Larger Ions



Next-generation batteries with high energy density rely on high-capacity electrode materials, but large volume changes and mechanical fracture in these materials during charge and discharge limit cycle life. Here, we discover that FeS<sub>2</sub> electrode materials are more mechanically resilient during reaction with larger alkali ions (sodium and potassium) compared with lithium, despite larger volume changes. These findings are important since they suggest that various large-volume-change electrode materials could enable stable cycling performance in next-generation sodium- and potassium-ion batteries.

Matthew G. Boebinger, David Yeh, Michael Xu, ..., Shuman Xia, Ting Zhu, Matthew T. McDowell  
mattmcowell@gatech.edu

## HIGHLIGHTS

*In situ* TEM reveals reaction mechanisms in FeS<sub>2</sub> with various alkali ions

Only reaction with lithium causes fracture

Fracture process is driven by evolution of crystal shape and stress concentrations

Finite element modeling and nanoindentation provide insight into chemomechanics

Article

# Avoiding Fracture in a Conversion Battery Material through Reaction with Larger Ions

Matthew G. Boebinger,<sup>1</sup> David Yeh,<sup>1</sup> Michael Xu,<sup>1</sup> B. Casey Miles,<sup>1</sup> Baolin Wang,<sup>2</sup> Marc Papakyriakou,<sup>2</sup> John A. Lewis,<sup>1</sup> Neha P. Kondekar,<sup>1</sup> Francisco Javier Quintero Cortes,<sup>1</sup> Sooyeon Hwang,<sup>3</sup> Xiahua Sang,<sup>4</sup> Dong Su,<sup>3</sup> Raymond R. Unocic,<sup>4</sup> Shuman Xia,<sup>2</sup> Ting Zhu,<sup>1,2</sup> and Matthew T. McDowell<sup>1,2,5,\*</sup>

## SUMMARY

Conversion and alloying electrode materials offer high specific capacity for emerging sodium- and potassium-ion batteries, but the larger volume changes compared to reaction with lithium are thought to limit cyclability. The reaction mechanisms of many materials with  $\text{Na}^+$  and  $\text{K}^+$  are unknown, however, and this knowledge is key for engineering mechanically resilient materials. Here, *in situ* transmission electron microscopy is used to uncover the nanoscale transformations during the reaction of  $\text{FeS}_2$  electrode materials with  $\text{Li}^+$ ,  $\text{Na}^+$ , and  $\text{K}^+$ . Surprisingly, despite larger volume changes during the conversion reaction with  $\text{Na}^+$  and  $\text{K}^+$ , the  $\text{FeS}_2$  crystals only fracture during lithiation. Modeling of reaction-induced deformation shows that the shape of the two-phase reaction front influences stress evolution, and unique behavior during lithiation causes stress concentrations and fracture. The larger volume changes in Na- and K-ion battery materials may therefore be managed through understanding and control of reaction mechanisms, ultimately leading to better alkali-ion batteries.

## INTRODUCTION

Due to the rapid growth of the electric vehicle and renewable energy markets, demand for energy storage with advantages in cost, cyclability, and/or energy density compared with Li-ion systems is increasing.<sup>1–4</sup> The emerging sodium-ion<sup>5,6</sup> and potassium-ion<sup>7,8</sup> battery systems, which contain different alkali metal ions, are promising alternatives. These battery systems offer the advantage of decreased materials costs, as Na and K are ~1,000 times more abundant than Li.<sup>4</sup> Furthermore, the expensive copper current collectors used in Li systems can be replaced with lower-cost and lighter-weight aluminum in Na-based systems due to the lack of alloying between Na and Al. Since  $\text{Na}^+$  and  $\text{K}^+$  are both monovalent, these systems offer the additional advantage of cell chemistries that are similar to Li-ion systems, and the vast trove of Li-related research is available to guide materials synthesis, characterization, testing, and deployment.

Recent research on Na-ion battery technologies has resulted in the development of a variety of anode and cathode materials with appropriate operating potentials and cycle life.<sup>3,4</sup> These materials undergo various types of reactions, including intercalation, alloying, and conversion.<sup>3,4,9–11</sup> While the specific energy of Na-based batteries is generally lower than that of Li-ion batteries, various combinations of anode

## Context & Scale

High-capacity electrode materials hold promise for next-generation batteries with high energy density. However, such materials often undergo large volume changes during charge and discharge, which can cause mechanical degradation and reduced cycle life. It is therefore critical to understand and control coupled reaction and degradation processes in high-capacity electrode materials. Here we find that  $\text{FeS}_2$ , a battery electrode material that undergoes a conversion-type reaction, fractures during reaction with lithium, but not with larger alkali ions (sodium and potassium). This result is counterintuitive, since larger ions induce larger volume changes, which are generally associated with greater stresses and more significant mechanical degradation. These findings are important since they indicate that large-volume-change electrode materials can be mechanically resilient in emerging sodium- and potassium-ion battery systems, which is a key aspect of attaining long cycle life.

and cathode materials can produce specific energies that are competitive with Li systems.<sup>2,9</sup> Although Na<sup>+</sup> has been the primary alternative alkali ion to receive attention for batteries, K<sup>+</sup>-based batteries may also allow for significant cost advantages. K-ion battery systems have recently begun to be explored due to the comparable standard potentials of the K/K<sup>+</sup> and Li/Li<sup>+</sup> redox couples (−2.93 V and −3.04 V versus the standard hydrogen electrode [SHE], respectively), as well as the natural abundance of K.<sup>7,8,10,12–14</sup> However, K-ion battery research is in a nascent stage, and most studies have only investigated carbon-based electrodes.<sup>7,8,12</sup> For continued development of these battery systems, it is critical to understand how reactions in various electrode materials proceed with different alkali ions; this knowledge can then be used to improve electrochemical behavior and reversibility of materials in these battery systems.<sup>8,10,12–16</sup>

While extensive research has been conducted on electrode materials that undergo large-volume-change alloying and conversion reactions in Li-based systems,<sup>17–21</sup> much less is known about how electrochemical reactions with other ions influence phase-transformation dynamics, electrochemical behavior, and mechanical degradation of active materials. Recent nanoscale engineering of battery electrode architectures to control morphological and volumetric changes in large-volume-change electrode materials for Li-ion batteries has yielded promising results.<sup>19,22</sup> However, due to the larger ionic radii of Na<sup>+</sup> and K<sup>+</sup> ions and the larger molar volume of Na- and K-based compounds, larger volumetric changes at similar capacity limits are expected during reaction with Na<sup>+</sup> and K<sup>+</sup> when compared with Li<sup>+</sup>.<sup>12,16</sup> Larger volumetric changes are generally associated with more substantial mechanical degradation and fracture of electrode materials,<sup>20,23,24</sup> which is thought to affect cycle life. However, the influence of these different ions on structural, morphological, and mechanical changes during reaction with various electrode materials is yet to be understood. To better engineer materials for maximized electrochemical performance in these emerging battery systems, the nanoscale reaction processes in Na- and K-ion battery electrode materials must be revealed.

Here, we investigate the dynamic nanoscale reaction mechanisms of an archetypal sulfide electrode material (FeS<sub>2</sub>) with three alkali-ion species (Li<sup>+</sup>, Na<sup>+</sup>, and K<sup>+</sup>) using a combination of *in situ* transmission electron microscopy (TEM), modeling, electrochemistry, and mechanical testing. FeS<sub>2</sub> is known to undergo a conversion-type reaction with Li,<sup>21,25,26</sup> and is a promising, high-capacity electrode material for multiple types of batteries, including primary Li cells.<sup>27</sup> It has been reported that FeS<sub>2</sub>-based secondary cells have relatively long cycle life in both Li- and Na-ion batteries (utilizing either partial reaction via intercalation or full conversion),<sup>25,27–31</sup> and FeS<sub>2</sub> electrodes have also shown promising high-capacity behavior in solid-state Li systems.<sup>26,28</sup> In this study, we show that the conversion reaction is active for all three alkali metal ions and that the phase transformation during discharge proceeds by a similar two-phase mechanism in each case. However, the mechanical integrity of individual FeS<sub>2</sub> nanocrystals was found to sharply diverge when reacting with different alkali metals. Interestingly, although lithiation causes smaller volume expansion than the reaction with Na<sup>+</sup> or K<sup>+</sup>, fracture only occurred during reaction with Li<sup>+</sup>. This unexpected behavior is due to fundamental differences in the evolution of the reaction front shape during reaction with the alkali ions, and could also be influenced by different mechanical properties of the reacted phases. These results indicate that despite larger volume changes, unforeseen nanoscale reaction pathways may mitigate mechanical degradation and allow for the effective use of conversion and alloying materials for rechargeable Na- and K-based batteries.

<sup>1</sup>School of Materials Science and Engineering, Georgia Institute of Technology, Atlanta, GA 30332, USA

<sup>2</sup>George W. Woodruff School of Mechanical Engineering, Georgia Institute of Technology, Atlanta, GA 30332, USA

<sup>3</sup>Center for Functional Nanomaterials, Brookhaven National Laboratory, Upton, NY 11973, USA

<sup>4</sup>Center for Nanophase Materials Sciences, Oak Ridge National Laboratory, Oak Ridge, TN 37831, USA

<sup>5</sup>Lead Contact

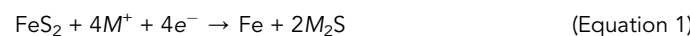
\*Correspondence: mattmcdowell@gatech.edu  
<https://doi.org/10.1016/j.joule.2018.05.015>

## RESULTS AND DISCUSSION

### Nanoscale Reaction Mechanisms with Li<sup>+</sup>, Na<sup>+</sup>, and K<sup>+</sup>

FeS<sub>2</sub> nanocrystals were used for *in situ* TEM investigations; these crystals were synthesized via a previously reported method that produces cube-shaped nanocrystals with relatively uniform size (see [Experimental Procedures](#) for details).<sup>32</sup> These nanocrystals were used as the active material for *in situ* TEM experiments to observe electrochemical reactions with various alkali ions. These experiments utilized a specimen holder ([Figure 1A](#)) that features a metallic probe that can be positioned to physically contact a TEM half-grid with FeS<sub>2</sub> nanocrystals dispersed on the surface. A small amount of the alkali metal of interest attached to the tip of a tungsten probe was brought into contact with the grid or nanocrystals, and a bias was applied to induce the electrochemical reactions with the alkali ions. The [Experimental Procedures](#) section contains complete experimental information.

An unreacted FeS<sub>2</sub> nanocrystal is shown in [Figure 1B](#), and the associated fast Fourier transform (FFT) is displayed in [Figure 1C](#). The FFT shows that the material is cubic pyrite (ICDD 04-004-6511, space group Pa $\bar{3}$ ), and the crystal is viewed along the [100] zone axis. Thus, the faces of these cube-shaped nanocrystals are the {100} crystallographic planes. A selected area electron diffraction (SAED) pattern from a collection of pristine FeS<sub>2</sub> nanocrystals is shown in [Figure 1H](#). The pyrite structure consists of a face-centered cubic sublattice of Fe, and each Fe atom is surrounded by six S nearest neighbors in a distorted octahedral arrangement.<sup>31</sup> Each S is bonded to another S atom as well as three Fe atoms, and the formal oxidation states of each element are Fe<sup>2+</sup> and S<sub>2</sub><sup>2-</sup>. The electrochemical conversion reaction of FeS<sub>2</sub> with alkali metal ions is expected to behave according to the following equation:



where M is the alkali metal of interest. The full conversion to M<sub>2</sub>S would involve electrochemical reduction of both the Fe<sup>2+</sup> cation and the S<sub>2</sub><sup>2-</sup> species. Lithium conversion reaction processes are known to produce biphasic structures with finely interspersed metal and sulfide or oxide phases after reaction.<sup>11,21,33,34</sup> While Li<sup>+</sup> and Na<sup>+</sup> are known to react with FeS<sub>2</sub> via a conversion mechanism,<sup>21,29</sup> the mechanism during reaction with K<sup>+</sup> has not been reported.

The nanoscale lithiation reaction of FeS<sub>2</sub> nanocrystals was examined first. [Figures 1D–1G](#) show two cubic FeS<sub>2</sub> crystals reacting with Li<sup>+</sup>. These data are also displayed in [Video S1](#). The lithiation of these particles progressed via the movement of a sharp reaction front between the internal FeS<sub>2</sub> crystal (the darker region) and the outer reacted phase with expanded volume (the lighter region). The shape of the shrinking internal FeS<sub>2</sub> crystal during the reaction process remained approximately cubic within both the large and small crystals ([Figures 1E](#) and [1F](#)). As the internal FeS<sub>2</sub> continued to react, a crack initiated at the bottom-right corner of the larger crystal ([Figure 1F](#)), and by the end of lithiation the larger particle had fractured at multiple locations to form a cluster of reacted fragments ([Figures 1F](#) and [1G](#)). The smaller particle also fractured at the upper-left corner. [Figure 1G](#) shows the material after full reaction of the larger particle; the center of the larger particle exhibits darker contrast because it is thicker in this region.

The lithiated phase that formed during the reaction process is a biphasic structure consisting of Li<sub>2</sub>S and Fe phases intermixed at the nanoscale. This structure is evident in the speckled contrast of the reacted region in [Figures 1E–1G](#); the darker specks correspond to nanoscale Fe particles, in agreement with prior work.<sup>21</sup> Before

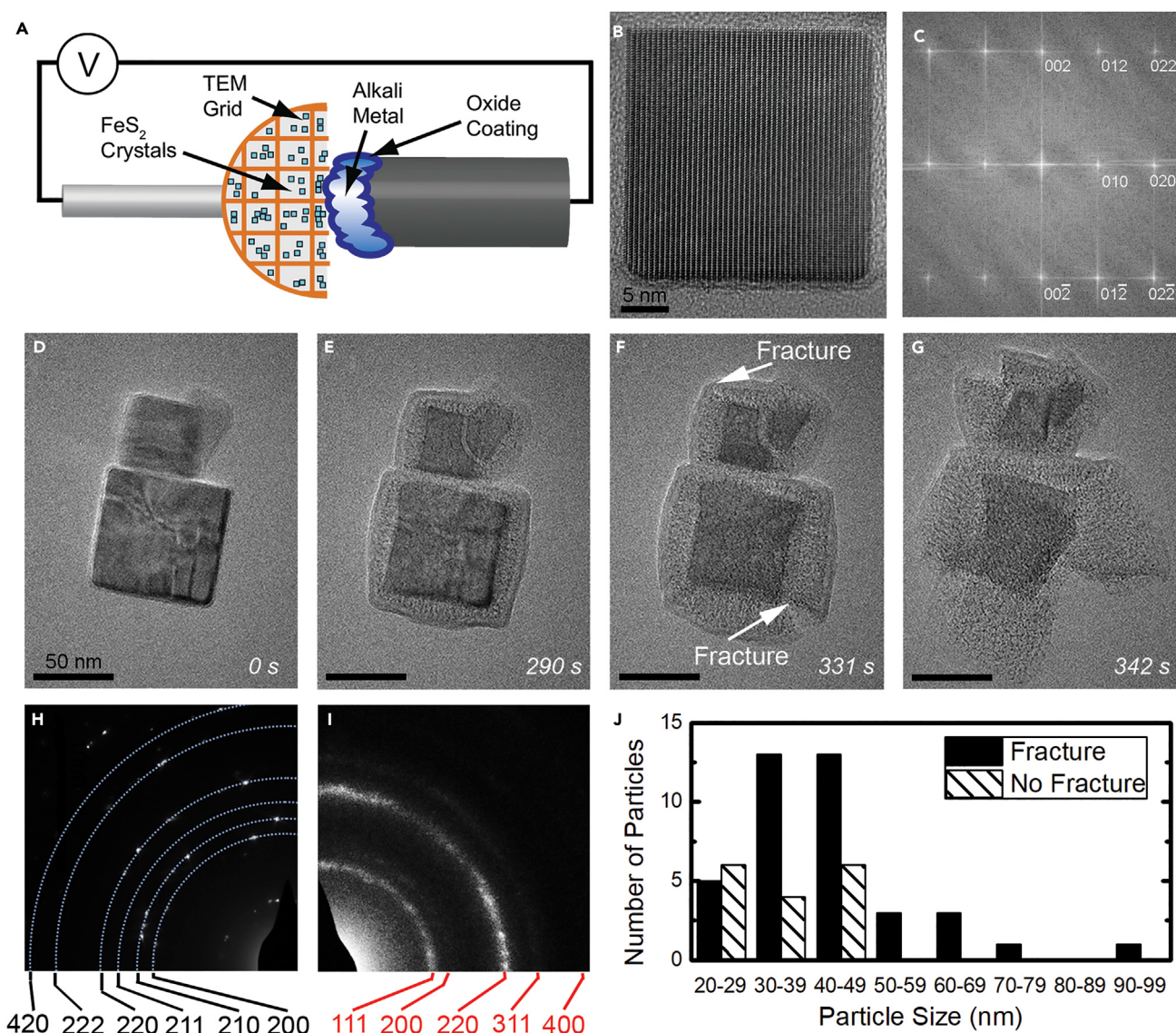


**Figure 1. The Reaction of FeS<sub>2</sub> with Lithium**

(A) Schematic of the *in situ* TEM experimental setup.

(B) High-resolution TEM image of an individual unreacted cubic FeS<sub>2</sub> crystal.

(C) The fast Fourier transform (FFT) of the unreacted FeS<sub>2</sub> crystal in (B) showing that the material is cubic pyrite viewed along the [100] zone axis.

(D–G) Snapshots of the lithiation of two FeS<sub>2</sub> nanoparticles. (D) The particles prior to reaction with lithium. (E) Lithiation has begun, and a sharp reaction front is visible between the internal FeS<sub>2</sub> crystal and the reacted mixture of Li<sub>2</sub>S and Fe. (F) Cracks have formed at the bottom-right corner of the larger crystal and the top-left corner of the smaller crystal. (G) The frame after full lithiation of the larger particle (the small particle still has FeS<sub>2</sub> within the interior); additional cracks have initiated and grown. The scale bars in (D)–(G) are 50 nm.

(H) The selected area electron diffraction (SAED) pattern of a group of pristine FeS<sub>2</sub> particles.

(I) The SAED pattern of the lithiated FeS<sub>2</sub> crystals showing broad rings corresponding to Li<sub>2</sub>S.

(J) A plot displaying the occurrence of fracture after lithiation as a function of the initial particle size.

the reaction, sharp FeS<sub>2</sub> diffraction spots were produced by the pristine material (Figure 1H). The SAED pattern of lithiated FeS<sub>2</sub> in Figure 1I shows broad rings that arise due to diffraction from Li<sub>2</sub>S, but no diffraction spots from body-centered cubic Fe were detected. A recent study used X-ray diffraction and pair distribution function analysis to conclude that the small Fe clusters produced through this electrochemical conversion reaction are in fact disordered,<sup>35</sup> which aligns with our observations.

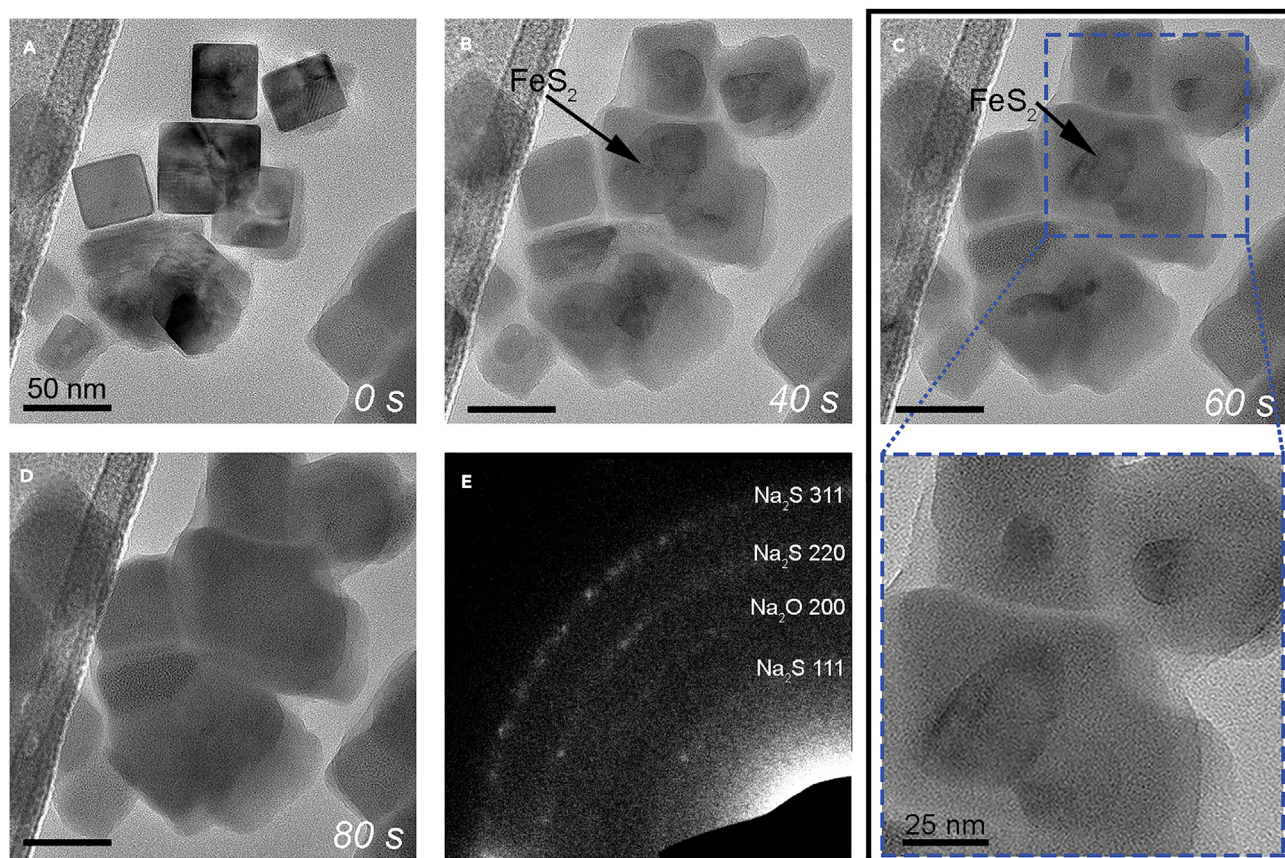


**Figure 2. Snapshots of the Sodiation of a Group of FeS<sub>2</sub> Particles**

- (A) Four unreacted FeS<sub>2</sub> particles are in the upper half of the frame, and the sodiation front is approaching from the lower-right corner of the frame.  
(B) The particles are shown in the midst of sodiation, and a sharp reaction front is visible between the unreacted crystals and the reacted phase. The scale bar is 50 nm.  
(C) Continuation of the sodiation reaction. The internal FeS<sub>2</sub> crystals within the particles have lost their initial shapes and have formed spherical or oblong shapes, as seen in the magnified inset. The scale bar in the upper frame is 50 nm.  
(D) All particles have reacted and the sodiated particles have merged together. The scale bar is 50 nm.  
(E) SAED pattern of the sodiated material showing diffuse rings that indicate the presence of Na<sub>2</sub>S and Na<sub>2</sub>O, which likely arises due to reaction of oxygen-containing groups on the surface of the carbon support.

High-resolution imaging of the reacted material revealed Li<sub>2</sub>S lattice fringes and Fe particles embedded within this Li<sub>2</sub>S matrix (Figure S1). From these images, the average size of the Fe particles in the matrix was  $1.0 \pm 0.25$  nm, and the separation between Fe particles was  $\sim 2.5$  nm. The theoretical volume expansion for the full conversion reaction is 2.6 (i.e., the volume of the final Li<sub>2</sub>S and Fe phases together is 2.6 times that of FeS<sub>2</sub>). It was difficult to estimate the volume expansion of most of the particles because of morphology changes due to fracture, but measurement of nine particles that did not fracture yielded an observed volume expansion of  $1.8 \pm 0.4$  after lithiation. The discrepancy between observed and theoretical volume expansion potentially arises due to incomplete reaction of the sulfur species. Finally, a plot that shows the occurrence of fracture as a function of particle size is shown in Figure 1J. Fracture was observed during lithiation for all sizes tested (between 20 nm and 100 nm), but some particles with initial size  $< 50$  nm did not fracture.

*In situ* TEM results from the sodiation of FeS<sub>2</sub> nanocrystals are shown in Figure 2, and Video S2 also shows this reaction process. In Figure 2A, crystals in the bottom-right

of the frame had already begun to react, since the Na species was diffusing along the carbon support from this direction. Sharp reaction fronts are visible between the interior FeS<sub>2</sub> regions and the reacted regions in Figures 2B and 2C during sodiation. The FeS<sub>2</sub> crystals in the interior of the particles did not retain cubic shapes during the reaction, as shown in the magnified inset of Figure 2C. The initially cubic FeS<sub>2</sub> crystals transformed to spherical or ellipsoidal shapes during the reaction, which suggests that the corners of the cubes react more readily to “round-off” sharp corners as the reaction occurs. This is in contrast to the lithiation case (Figure 1), in which crystals retained cubic shapes during the reaction. After the reaction was complete, the sodiated particles were observed to merge together (Figure 2D). However, unlike the lithiation case, fracture did not occur despite a measured average volume expansion of  $2.7 \pm 0.3$ . The theoretical volume expansion for the formation of Na<sub>2</sub>S and Fe is 3.8, which again suggests that some of the material undergoes incomplete reaction. After reaction (Figure 2D), contrast due to the two-phase mixture of Na<sub>2</sub>S and Fe particles was evident. The SAED pattern after sodiation in Figure 2E features weak rings corresponding to Na<sub>2</sub>S, indicating that the Na<sub>2</sub>S was present but had poor crystallinity. The resulting Fe particles were found to be approximately  $0.58 \pm 0.15$  nm in size, which is smaller than the lithiation case. The average Fe-Fe particle separation within the matrix was also smaller, at  $\sim 1.8$  nm.

The reaction of FeS<sub>2</sub> with K<sup>+</sup> was also examined with *in situ* TEM, and data from a typical experiment are shown in Figure 3 and Video S3. Figure 3A shows two overlapping FeS<sub>2</sub> crystals on the edge of the carbon support; the K probe is visible at the top of the frame. It was found that potassiation required direct contact to be made between the oxide/hydroxide layer on the surface of the K probe and the FeS<sub>2</sub> crystal, as shown in Figure 3B. This contact requirement was likely due to the slow diffusion of K<sup>+</sup> ions through the carbon support film, which is in contrast to the Li<sup>+</sup> and Na<sup>+</sup> cases. During contact and biasing in Figures 3A and 3B, the reaction initially progressed rapidly before slowing in Figures 3C and 3D. A sharp reaction front formed between the FeS<sub>2</sub> crystals and the reacted phase, which is similar to the lithiation and sodiation processes. During potassiation, the “rounding-off” of the corners of the FeS<sub>2</sub> crystal was also evident, as shown in Figure 3C. After full reaction (Figure 3D), fracture did not occur despite the large average volume expansion of  $3.1 \pm 0.6$ , as measured across many experiments. As in the lithiation and sodiation cases, this observed volume expansion is lower than the theoretically predicted value of 5.4. The SAED pattern of the final reacted phase in Figure 3E shows a diffuse ring that corresponds to an amorphous product. No image contrast from separate Fe and potassium sulfide phases was evident, indicating a single-phase amorphous product that contains K, Fe, and S.

This investigation of the reaction process with all three alkali ions under similar conditions allows for valuable comparisons to be made regarding reaction mechanisms. Multiple aspects of these reactions behave according to rational trends when moving from Li<sup>+</sup> to K<sup>+</sup>. For instance, it was found that the average size of the Fe particles in the product phase decreased as the alkali-ion size increased. In tandem with this observation, the crystallite size of the alkali sulfide product also decreased with increasing alkali-ion size. In all cases, the particle size in the product phase did not change after initial reaction and it did not depend on FeS<sub>2</sub> crystal size. The formation of the product phase at the reaction front likely involves the short-range migration of Fe atoms to form clusters as the alkali sulfide is formed around it. The decrease in Fe particle size when reacting with larger ions therefore indicates that the size and/or mobility of the alkali ion influences the extent to which Fe is able to migrate to form clusters, with the smallest ion (Li<sup>+</sup>) enabling the most facile migration. In

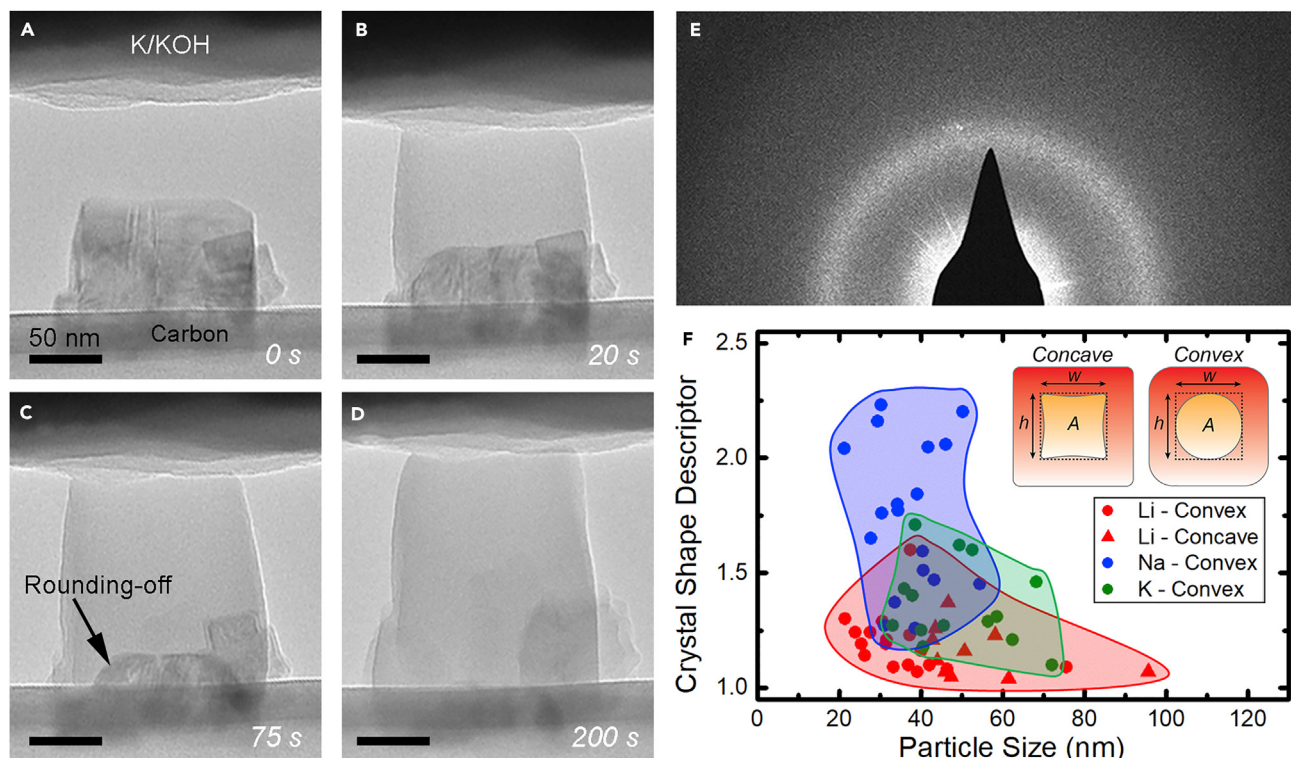


**Figure 3. Potassiation of  $\text{FeS}_2$  and Reaction Statistics**

(A–D) Snapshots of the potassiation of  $\text{FeS}_2$ . (A) A pristine  $\text{FeS}_2$  particle with a smaller overlapping particle on the right side. (B) Potassiation has begun after contact and biasing, and a sharp reaction front between the lighter reacted phase and the  $\text{FeS}_2$  crystal is evident. (C) An image after further reaction; the edges of the  $\text{FeS}_2$  crystal are blunted. (D) Image after full reaction of the  $\text{FeS}_2$ . The scale bars in (A)–(D) are 50 nm.

(E) The SAED pattern of the final reacted amorphous product.

(F) A plot that quantifies the extent of change of the  $\text{FeS}_2$  crystal shape during reaction with the different alkali ions. The crystal shape descriptor,  $Y$ , is defined as  $Y = wh/A$ , where  $wh$  is the rectangular area in which the crystal is inscribed and  $A$  is defined as the actual  $\text{FeS}_2$  crystal area. A number greater than 1.0 is associated with a more spherical or oval crystal shape.

addition to this trend, the magnitude of volume expansion increased with alkali-ion size, as expected. Finally, it was observed that all three alkali-ion species reacted with  $\text{FeS}_2$  via a two-phase reaction with an associated sharp reaction front; this indicates that the reaction kinetics is controlled by short-range interactions and bond breaking near the reaction front. Two-phase reactions also occur in other large-volume-change battery materials such as Si and Ge.<sup>36–39</sup>

#### Linking Fracture to Phase-Transformation Processes

In contrast to these other trends, the morphology changes and fracture processes observed herein are difficult to rationalize based on the size and mobility of the alkali ions alone. In the dozens of particles studied for each alkali species, fracture only occurred during lithiation (images of other particles during reaction are shown in Figures S2–S4). Fracture did not occur during either sodiation or potassiation regardless of particle size (the largest particles that were tested were  $\sim 120$  nm) and despite the larger volumetric expansions associated with these reactions. This is counterintuitive, as larger volume expansion is generally associated with greater stress values that could more effectively drive crack formation. Since fracture has been linked to electrochemical degradation processes in batteries,<sup>40–42</sup> these observations have implications for the beneficial use of  $\text{FeS}_2$  in Na- and K-based systems. However, the question remains regarding the cause of this divergent fracture behavior.

One factor that likely contributes to the observed differences in fracture behavior is the evolution of the shape of the reaction front during reaction. During lithiation, the internal crystalline FeS<sub>2</sub> generally maintained a square or rectangular shape throughout the reaction process; in other words, the {100} planes of the crystal structure were maintained at the reaction front. As previously discussed, the corners of the FeS<sub>2</sub> crystals became blunted during sodiation and potassiation, leading to crystals that were circular or oblong (in projection) during reaction. This indicates that the {100} planes did not preferentially exist at the reaction front. To provide statistical evidence for these observations across many tested particles and to quantify the extent of crystal shape changes, Figure 3F is a plot that captures the shape of the internal FeS<sub>2</sub> crystals during reaction as a function of particle size. Each data point in the plot is from a distinct particle, which illustrates the generality of the observations presented in Figures 1–3. These points are from the subset of particles in which the internal crystal shape during the reaction was able to be measured. The “crystal shape descriptor” is plotted on the y axis; this value is defined as the rectangular area in which the crystal is inscribed, divided by the actual area of the FeS<sub>2</sub> crystal. Based on the inset schematics in Figure 3F for crystals surrounded by reacted material, the crystal shape descriptor Y would be calculated as  $Y = wh/A$ , where  $wh$  is the square or rectangular area in which the crystal is inscribed and  $A$  is defined as the actual FeS<sub>2</sub> crystal area. Thus, for crystals that retain a rectangular shape during reaction, the shape descriptor would remain close to 1.0. For crystals that transform into spherical or oval shapes, the shape descriptor would be larger. The plot in Figure 3F shows the maximum crystal shape descriptor during the reaction.

The data in Figure 3F show that, across all experiments, reaction with different alkali species resulted in quantitatively different internal crystal shapes. Lithiation resulted in crystal shape descriptor values that were close to 1.0 (generally less than 1.35) across all sizes, which indicates that the crystals retained shapes that were close to rectangular or square. The crystal shape descriptor values for sodiation were higher than those for lithiation (ranging between ~1.25 and ~2.25), while the values for potassiation fell between the other two cases (ranging between ~1.10 and ~1.70). Thus, sodiation featured the most extensive transformation to oval and circular crystal shapes. It should be noted that irregular oval shapes led to high crystal shape descriptor values around 2.0. Finally, for the lithiation case, crystals that evolved to take either convex or concave shapes were observed (see the schematic inset in Figure 3F). The concave shape only appeared when particles exceeded about 45 nm in size.

It is clear that the different alkali ions caused different internal crystal shapes to evolve during reaction. These variations can be attributed to differences in the atomic-scale dynamics of bond breakage at the reaction front between the reacted material and the FeS<sub>2</sub> crystal. The square or rectangular shapes during lithiation are due to preferential reaction of the {100} planes of the FeS<sub>2</sub> crystal, which results in the retention of these facets at the reaction front. This suggests that the kinetics of the reaction in these small particles is interface-limited, as is seen in other large-volume-change materials.<sup>39</sup> The preferential lithiation of the {100} planes likely occurs due to a favorable atomic arrangement at these planes that promotes reaction with Li<sup>+</sup>. In contrast, the lack of sharp facets during reaction with Na<sup>+</sup> and K<sup>+</sup> indicates that the {100} planes do not react preferentially, even though the kinetics are likely still interface-limited. The “rounding-off” or blunting of corners during sodiation and potassiation could be caused by higher concentrations of alkali ions available for reaction near the corners/edges due to increased ion transport pathways from the particle surface at these locations, which could influence interfacial reaction rates.

This suggests that blunting of corners naturally arises in the absence of planes of preferential reaction in such two-phase-transformation processes.

The evolution of crystal shape and the occurrence of fracture are likely related. Fracture was observed only during reaction with lithium, and lithiation was the only case in which the internal crystal shape remained as a square or rectangle. Interestingly, cracks were often observed to initiate at corners of the nanocrystals during lithiation. These observations suggest that the highly anisotropic expansion of the FeS<sub>2</sub> during lithiation is related to the fracture process. The preferential expansion at cube faces during lithiation causes tensile stress concentrations at the surface between reacting faces (i.e., at the corners), which could cause cracks to preferentially initiate at the corners. Prior work has been performed to describe the stress state within particulate battery materials during two-phase, large-volume-change reactions such as that observed here in FeS<sub>2</sub>.<sup>18,20,23,24,43</sup> The reacted product phase near the reaction front experiences significant compressive stress, while the surface of the particle experiences tensile stress. Previous work has also demonstrated that anisotropic expansion of a material during electrochemical reaction can dramatically influence the fracture behavior. Specifically, fracture preferentially occurred at the surface of crystalline Si nanopillars between preferentially expanding crystal facets.<sup>17,18,22</sup> In contrast, amorphous Si has been observed to undergo isotropic expansion, and it is much more resistant to fracture.<sup>44</sup> Therefore, our observation of fracture at the corners of FeS<sub>2</sub> cubes during lithiation is consistent with prior work, but the differences among different alkali ions have not been observed.

These experiments also provide information related to rate and size effects on fracture. The fracture process for the two-phase reactions reported here appears to be insensitive to reaction rate or phase-transformation kinetics. This is because the evolved stress depends primarily on the extent of reaction, since the concentration of alkali ions in the reacted phase is approximately constant.<sup>24</sup> Reaction rates were generally faster for lithiation compared with sodiation and potassiation, but rates also varied among different particles for a given alkali ion (Figure S5 shows plots of reaction kinetics). However, only lithiation (with varying reaction rates) resulted in fracture, indicating that reaction kinetics do not play a significant role in the fracture process. Regarding size effects on fracture, some smaller lithiated FeS<sub>2</sub> crystals avoided fracture (as shown by the statistics in Figure 1J). This is consistent with prior research, as similar size dependence for fracture during the first lithiation has also been reported for nanoscale crystalline Si particles and wires. For Si, however, fracture can be avoided altogether for sizes less than ~150 nm.<sup>18,45</sup> In general, smaller particles contain less total deformation-induced strain energy to drive the formation of new crack surfaces, which reduces the probability that the particles will fracture. This analysis suggests that regardless of the active ion used, there will be a critical size above which fracture will occur. For the sodium and potassium experiments discussed here, the critical size was evidently not reached. Beyond avoiding mechanical degradation, the use of very small (~5 nm) FeS<sub>2</sub> crystals has previously been suggested to be beneficial for long-term cycling because the particle size is on the same length scale as the diffusion length of Fe during reaction, enabling facile conversion.<sup>25</sup> Thus, both chemical and mechanical aspects of electrochemical reactions must promote stability for effective long-term cycling.

### Modeling Stress Evolution during Reaction

To quantify the effects of crystal shape evolution on stress during reaction, we carried out chemomechanical simulations using the finite element method to model concurrent ion transport, reaction front migration, volume expansion, and stress

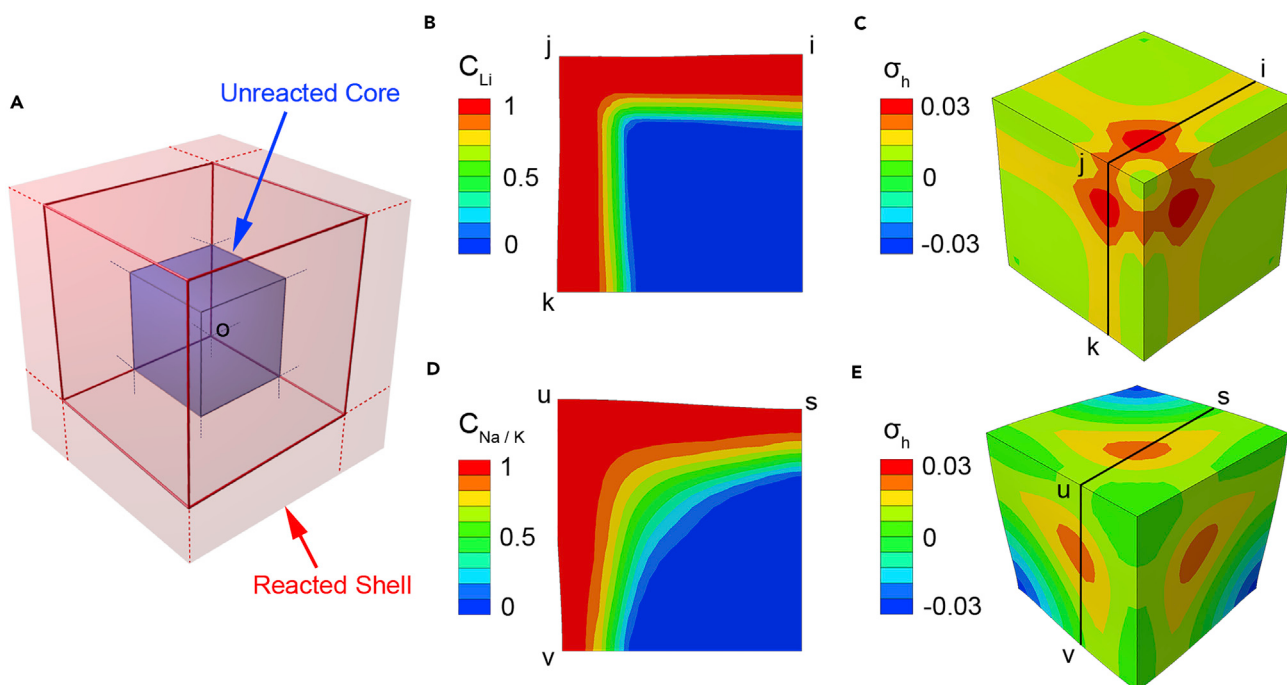


**Figure 4. Chemomechanical Finite Element Simulation Results Showing Stress Generation during Reaction of a Cubic  $FeS_2$  Particle with Different Reaction Front Shapes**

(A) Schematic of two-phase lithiation/sodiation, with a sharp reaction front (colored blue) between a cubic unreacted core and a lithiated/sodiated shell (colored red). Only one-eighth of the cubic particle is modeled (outlined by the solid red lines), given the symmetry of the reaction and stress generation processes. The “o” symbol marks the center of the full cubic particle.

(B and C) Simulation results of the reaction when the inner crystal retains a cubic shape with a sharp corner (i.e., the lithiation case). A contour plot of Li concentration  $C_{Li}$  (normalized by the concentration of Li at the full extent of lithiation) at a representative cross-section is shown in (B), and a contour plot of hydrostatic tensile stress  $\sigma_h$  (normalized by Young’s modulus) is shown in (C). The position of the cross-section in (B) is marked by the black lines in (C). (D and E) Simulation results of the reaction when the inner crystal develops a rounded-off or blunted corner (i.e., sodiation or potassiation). A contour plot of ion concentration  $C_{Na/K}$  at a representative cross-section is shown in (D), and a contour plot of hydrostatic tensile stress  $\sigma_h$  (normalized by Young’s modulus) is shown in (E). The cross-section in (D) is marked in (E).

generation. These simulations captured the two-phase reaction at sharp phase boundaries through the use of concentration-dependent diffusivity, as previously demonstrated.<sup>46</sup> To specifically compare the effects of reaction front shape on stress evolution, simulations were carried out with the same volumetric expansion (using a representative volume expansion value of 2.2) but with different reaction front shapes. Since the magnitude of volume expansion influences stress evolution, simulating the same volume expansion enables direct comparison of the effects of reaction front shape. Full simulation details are included in [Experimental Procedures](#).

Chemomechanical simulation results are shown in [Figure 4](#) for a cubic particle in the midst of reaction. Considering the symmetry of reaction and stress generation with respect to the {100} cube faces, we only modeled one-eighth of a cube, as schematically shown in [Figure 4A](#). Here, the red outer boundary represents the particle surface and the blue internal boundary approximates the position of the reaction front; the solid red lines denote the boundary of the modeled region. [Figures 4B](#) and [4C](#) show simulation results for the case of lithiation, in which the reaction front is aligned with the {100} facets and the unreacted crystalline core has sharp corners. The contour plot of the normalized Li concentration in [Figure 4B](#) shows that there is a sharp increase in Li concentration at the reaction front, and three mutually perpendicular {100} reaction fronts intersect to form a sharp corner of the unlithiated core.

A contour plot of the lithiation-induced hydrostatic tensile stress is shown in [Figure 4C](#). Note that the hydrostatic tension becomes the in-plane tension near free surfaces, such that its contour plot can effectively reveal the three-dimensional, symmetric distribution of surface tensile stresses around a corner of the cubic particle. [Figure 4C](#) shows that large tensile stress concentrations arise around the surface locations that coincide with the underlying sharp corner of the un lithiated core, and they are induced by the large expansion near the intersecting {100} reaction fronts during lithiation. Such stress concentrations can drive fracture at the edge or corner of FeS<sub>2</sub> particles, as observed during *in situ* TEM experiments. In contrast, [Figures 4D and 4E](#) show simulation results for the case of reaction front evolution with a "blunted" reaction front shape (as is the case with sodiation and potassiation). The contour plot of the normalized Na concentration ([Figure 4D](#)) shows that the corner of the unreacted crystal core has been rounded off to feature a less-sharp reaction front angle. The corresponding contour plot of the hydrostatic tensile stress is shown in [Figure 4E](#). Comparing [Figures 4C and 4E](#), the stress concentrations at the particle surfaces are weaker for the rounded reaction front (sodiation or potassiation) compared with the sharper corner (lithiation). This manifests as tensile stress that is more spatially distributed and lower in magnitude ([Figure 4E](#)). These simulations are consistent with the TEM observation of fracture in lithiated FeS<sub>2</sub> particles as opposed to the lack of fracture in sodiated and potassiated FeS<sub>2</sub> particles. [Table S1](#) contains values of the maximum tensile stress during reaction for both cases, and these data show that the cubic reaction front produces higher stresses throughout the reaction.

In addition to the effect of reaction front shape on fracture processes, the mechanical properties of the lithiated, sodiated, and potassiated materials may be different, which could also influence fracture characteristics. While the mechanical properties (e.g., yield strength, elastic modulus) of a number of different lithium alloy materials have been measured,<sup>20,40,47–49</sup> the mechanical properties of conversion materials, as well as Na and K electrode materials, have been less studied. To gain a basic understanding of the mechanical properties of electrochemically reacted FeS<sub>2</sub>, we carried out nanoindentation experiments. FeS<sub>2</sub> thin films were electrochemically reacted in half cells, and the reacted films were removed and indented within an argon-filled glovebox. As shown in [Figure S6](#), the lithiated FeS<sub>2</sub> film exhibited slightly lower elastic modulus but similar hardness compared with the sodiated and potassiated material. Thus, the three materials should flow at similar stress values. Since lithium was the only alkali ion to induce fracture in the nanocrystals during reaction, these findings suggest that the previously described stress intensification due to anisotropic lithiation plays a significant role in causing crack formation, rather than differences in mechanical properties. However, comprehensive mechanical investigation of these materials must be undertaken to fully understand the effects of mechanical properties; for instance, measurement of fracture toughness is necessary. Furthermore, electrochemical potassiation may not result in full reaction (as detailed in [Figure 5](#)), so these samples may exhibit mechanical properties slightly different from those of fully potassiated FeS<sub>2</sub>.

### Electrochemical Behavior of FeS<sub>2</sub> in Half Cells

As a final aspect of this study, the discharge behavior of FeS<sub>2</sub>-based active electrodes in electrochemical half cells was examined for comparison to the *in situ* TEM results. These cells were fabricated with alkali metal counter electrodes and commercial FeS<sub>2</sub> powder in the working electrodes, along with organic electrolytes containing different alkali metal salts (see [Supplemental Information](#) for complete

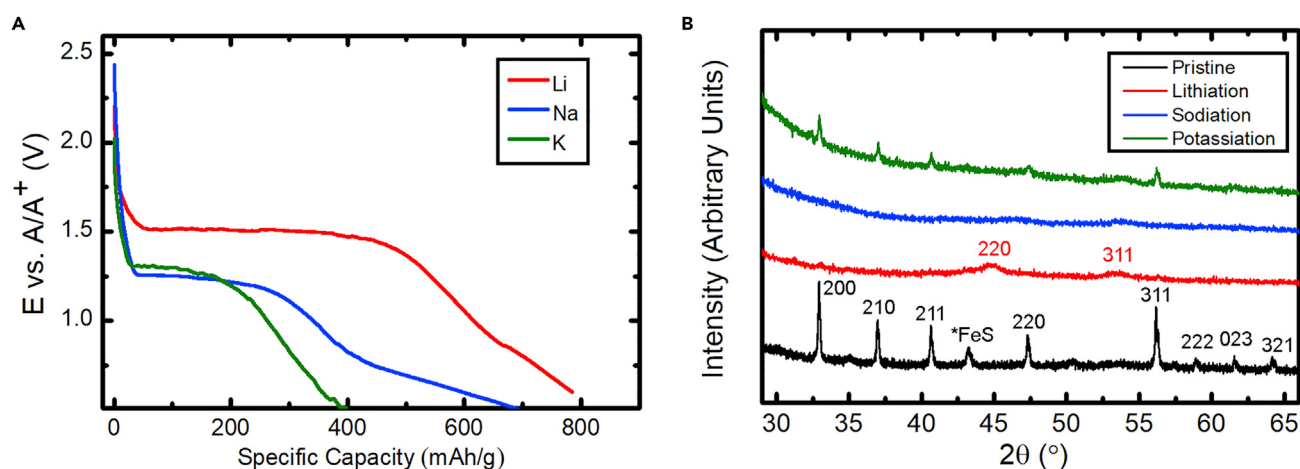


**Figure 5. Electrochemistry of FeS<sub>2</sub> in Half Cells**

(A) Galvanostatic discharge curves for FeS<sub>2</sub> electrodes in Li, Na, and K half cells at a rate of C/20 (full discharge in 20 hr). The discharge curves are plotted on the same graph with different potential ( $E$ ) scales, where  $A/A^+$  corresponds to  $Li/Li^+$ ,  $Na/Na^+$ , and  $K/K^+$ .

(B) Ex situ XRD of FeS<sub>2</sub> electrodes before and after discharge in Li, Na, and K half cells. The spectrum from the pristine material shows mostly FeS<sub>2</sub> peaks with a FeS secondary phase.

details). Figure 5A shows the galvanostatic discharge curves from Li, Na, and K half cells. All three discharge curves show relatively flat initial plateaus at different potential values, followed by sloping sections. The Li discharge behavior is consistent with prior studies, some of which have also reported an additional higher-potential plateau at slow discharge rates.<sup>27</sup> The discharge of the Li cell shows the longest plateau, while the Na and K cells exhibit shorter plateaus. These flat potential plateaus in all three cases indicate two-phase reactions, which correspond to the two-phase reactions and sharp reaction fronts that were directly observed in the *in situ* TEM experiments. Importantly, this correlation indicates that although the *in situ* observations were performed in a vacuum environment, the observed phase transformations are likely similar to or the same as those exhibited in true electrochemical cells (as has previously been demonstrated for other materials<sup>11,37</sup>). The standard potentials of  $Li/Li^+$ ,  $Na/Na^+$ , and  $K/K^+$  are  $-3.04$  V,  $-2.71$  V, and  $-2.93$  V, respectively, versus SHE. Since the initial plateaus in the galvanostatic curves are at different potentials in Figure 5A, this suggests that the energetics of the two-phase reaction are similar for all three cases, with the varying standard potentials of the alkali metal redox couples influencing the positions of the plateaus. The two-phase mechanism is active for all three cases even though the potassium reaction results in an amorphous reacted phase. Finally, the theoretical specific capacity for the reaction of FeS<sub>2</sub> to form Fe and the associated alkali metal sulfide is  $894$  mAh g<sup>-1</sup> in all three cases. Figure 5A shows that the Li cell comes the closest to this theoretical capacity, and as the size of the alkali metal ion increases, the specific capacity decreases. This may be due to kinetics limitations due to the larger ionic size of Na<sup>+</sup> and K<sup>+</sup>.

The overall phase evolution of the FeS<sub>2</sub> active material in these electrochemical cells was also similar to that observed with *in situ* TEM. Figure 5B shows ex situ X-ray diffraction (XRD) data from a pristine electrode and electrodes after discharge in Li, Na, and K cells. The pristine commercial FeS<sub>2</sub> material (black trace) displayed Bragg peaks corresponding to cubic pyrite, as well as a minor FeS phase component. After lithiation (Figure 5B, red), all the sharp FeS<sub>2</sub> peaks disappeared and broad, weak peaks associated with Li<sub>2</sub>S (ICDD 04-008-3440) emerged,

indicating that poorly crystalline Li<sub>2</sub>S was present after the reaction. Fe peaks were not visible. The XRD trace from the Na cell after discharge (Figure 5B, blue) also showed the disappearance of the FeS<sub>2</sub> peaks, but there were no observed crystalline reaction products. This indicates that the resulting Na<sub>2</sub>S, shown to result from this type of reaction from *in situ* TEM (Figure 2), is likely very poorly crystalline. After discharge in a K cell (Figure 5B, green), the FeS<sub>2</sub> Bragg peaks did not completely disappear, but only decreased in intensity while no other peaks appeared. This indicates that the active material did not fully react in the K cell, which is supported by the lower specific capacity of this cell compared with the other two. However, the decreased intensity of the peaks still shows that the electrochemical reaction of FeS<sub>2</sub> occurred in the K cell, which has not been reported before. The FeS<sub>2</sub> active material is likely undergoing a conversion reaction under electrochemical conditions, which suggests that the *in situ* TEM experiments also show realistic phase evolution.

## Conclusions

This study has revealed the different nanoscale reaction pathways that occur during lithiation, sodiation, and potassiation of FeS<sub>2</sub> using a combination of *in situ* TEM, chemomechanical modeling of stress evolution, electrochemistry, and mechanical testing. FeS<sub>2</sub> nanocrystals were observed to undergo conversion-type reactions via a two-phase mechanism with the movement of a sharp reaction front in all cases. The key result of this study is that despite significantly larger volume changes during sodiation and potassiation, particles were only observed to fracture during lithiation. This result runs counter to conventional wisdom suggesting that larger volume changes in battery materials necessarily lead to larger stresses and more significant mechanical degradation. The shape of the reaction front was quantified and was found to contribute to these differences in mechanical failure; the reaction front during lithiation was found to maintain a rectangular shape with {100} facets, while the reaction front during sodiation and potassiation evolved to an oval shape with blunted corners. Chemomechanical modeling of stress evolution showed that a rectangular phase front should lead to higher tensile stresses at the corners/edges of particles, which leads to fracture as observed in the lithiation case. It is also possible that differing fracture toughness of the various product phases contributes to the divergent fracture behavior.

These findings are important since they indicate that even though high-capacity alloying and conversion materials exhibit larger volume changes in Na-ion and K-ion battery systems compared with Li-ion systems, these volume changes may be manageable and do not necessarily induce particle failure. As demonstrated herein, it is critical to understand how detailed nanoscale reaction mechanisms influence morphological changes; this information can then be used to tailor the shape, size, and structure of materials for batteries. The discovery of the different nanoscale reaction pathways in FeS<sub>2</sub> crystals and how these pathways influence fracture is a critical step toward engineering these materials for use in next-generation Na- and K-based battery systems.

## EXPERIMENTAL PROCEDURES

### FeS<sub>2</sub> Nanocrystal Synthesis

FeS<sub>2</sub> nanocrystals were synthesized via a two-step solution-based process.<sup>32</sup> This procedure involves heating anhydrous FeCl<sub>2</sub> and elemental sulfur in alkyl-amines under nitrogen. Full experimental details are provided in [Supplemental Information](#).

## In Situ TEM

The *in situ* TEM experiments utilized an FEI NanoEX 3D TEM/STM specimen holder that allows for physical manipulation of nanoscale samples and electrical biasing. The holder features a metallic probe that can be positioned to physically contact a TEM half-grid, as seen in Figure 1A. FeS<sub>2</sub> nanocrystals were dispersed on a lacey carbon half-grid and inserted into the holder. A small amount of the alkali metal of interest was then attached to the tip of a tungsten probe in an argon-filled glovebox and the probe was then quickly removed from the glovebox and attached to the specimen holder, which was then inserted into the TEM column. During the transfer process, the alkali metal on the probe was exposed to air for less than 1 min, causing the growth of oxide, hydroxide, and/or nitride layers on the surface of the metal. Inside the microscope, the alkali metal-tipped probe was positioned to make contact with the carbon grid near a cluster of FeS<sub>2</sub> crystals for the Li and Na cases. For K reactions, FeS<sub>2</sub> crystals were directly contacted by the potassium oxide/hydroxide surface layers. A negative bias of –2.0 V was then applied to the grid with respect to the probe, causing alkali ions to be driven through the oxide/hydroxide surface layers and reduced at the carbon grid or FeS<sub>2</sub> crystals; in this way, the surface layers behave as a solid electrolyte and facilitate ion transport. In all cases, experiments were performed to determine the beam intensity that allowed for stable imaging of the reacted material. A beam spot size of 5 or greater was used. Furthermore, control experiments were performed on material that reacted while not exposed to the beam; the similar structure and morphology of the reaction product in these experiments indicated that the beam did not significantly influence the reaction pathway.

## Electrochemical Testing

Electrochemical data was obtained using CR2032 stainless-steel coin cells with FeS<sub>2</sub> working electrodes and lithium, sodium, or potassium metal foils used as the counter/reference electrode. The electrolytes used for the electrochemical tests were as follows: 1.0 M LiPF<sub>6</sub> in 1:1 (v/v) ethylene carbonate/diethyl carbonate, 1.0 M NaPF<sub>6</sub> in diethylene glycol dimethyl ether, and 1.0 M KPF<sub>6</sub> in a 1:1 (v/v) mixture of ethylene carbonate/diethyl carbonate. The cells were sealed using a hydraulic press within an Ar-filled glovebox with H<sub>2</sub>O level <2.0 ppm and O<sub>2</sub> level <1.0 ppm. Galvanostatic electrochemical discharge tests were performed on a Landt Battery Testing System at room temperature. The lower voltage limits were 0.6 V versus Li/Li<sup>+</sup> for Li/FeS<sub>2</sub> cells, 0.5 V versus Na/Na<sup>+</sup> for Na/FeS<sub>2</sub> cells, and 0.5 V versus K/K<sup>+</sup> for K/FeS<sub>2</sub> cells.

## X-Ray Diffraction

*Ex situ* XRD experiments of the FeS<sub>2</sub> electrode films were performed using a PANalytical Empyrean instrument with a Cu K<sub>α</sub> radiation source ( $\lambda_{K\alpha 1} = 1.54 \text{ \AA}$ ). After lithiation, sodiation, or potassiation, the FeS<sub>2</sub> electrodes were removed from their coin cell housings in an Ar-filled glovebox and rinsed with electrolyte solvent. The electrode material was scraped from the Cu foil current collector onto a glass slide that was then covered with a thin layer of Mylar and sealed with Kapton tape to avoid atmospheric exposure during the experiment.

## Chemomechanical Model and Finite Element Method Simulations

A chemomechanical model was developed to study the concurrent ion transport, reaction front migration, volume expansion, and stress generation in a cubic FeS<sub>2</sub> particle. These simulations captured the two-phase reaction at sharp phase boundaries through the use of concentration-dependent diffusivity.<sup>46</sup> The simulations were numerically implemented by using temperature as a surrogate for ion concentration in the commercial finite element package ABAQUS, since the governing transport

equations are identical.<sup>23,46</sup> In this implementation, thermal expansion stands in for chemical expansion. The [Supplemental Information](#) contains complete simulation details, including the values for material properties used.

#### Nanoindentation

FeS<sub>2</sub> thin films with thicknesses between 200 and 400 nm were grown by sulfurizing sputtered Fe films. Fe films were sputtered onto Ta foil substrates, and sulfurization was carried out in a tube furnace by heating the Fe films to 500°C while exposing them to sulfur vapor entrained in Ar flow. Sulfur powder was placed upstream of the Fe films in the tube furnace, and Ar was flowed at 40 sccm while the pressure was maintained at 1,200 mTorr.<sup>50</sup> These films were then directly used as working electrodes in Li, Na, and K half-cell-type coin cells. Discharge was performed using currents of C/20 with 0.6 V as the cell potential cutoff value ([Figure S7](#) shows typical thin-film discharge curves). After discharge, the working electrodes were removed in an Ar-filled glovebox with <0.1 ppm H<sub>2</sub>O and O<sub>2</sub> content, and the films were indented in the same glovebox using a Hysitron nanoindentation system with a Berkovich indenter tip. Residual liquid electrolyte was immediately removed from the film surfaces using Kimwipe tissues after extraction of the samples from the coin cells. All films were tested without washing with extra solvent to avoid delamination of films and to minimize the chance of excessive side reactions. Surface scanning with the indentation tip was utilized to identify relatively smooth regions for accurate indentation measurements. The pristine and reacted films demonstrated similar topographic morphology, suggesting minimal presence of a solid electrolyte interphase layer. A peak load of 40 μN at a constant loading/unloading rate of 8 μN·s<sup>-1</sup> was used during nanoindentation tests. For each film, data were collected from at least five indents conducted at different locations on the film to ensure the measurements were not affected by local morphological variations.

#### SUPPLEMENTAL INFORMATION

Supplemental Information includes Supplemental Experimental Procedures, seven figures, one table, and three videos and can be found with this article online at <https://doi.org/10.1016/j.joule.2018.05.015>.

#### ACKNOWLEDGMENTS

A portion of this research was conducted at the Center for Nanophase Materials Sciences, which is a DOE Office of Science User Facility (X.S. and R.R.U.). This research also used resources at the Center for Functional Nanomaterials, which is a US DOE Office of Science User Facility at Brookhaven National Laboratory, under contract no. DE-SC0012704 (S.H. and D.S.). This work was performed in part at the Georgia Tech Institute for Electronics and Nanotechnology, a member of the National Nanotechnology Coordinated Infrastructure, which is supported by the National Science Foundation (grant ECCS-1542174). This material is based upon work partially supported by the National Science Foundation under award nos. DMR-1652471, DMR-1410936, and CMMI-1554393.

#### AUTHOR CONTRIBUTIONS

M.G.B. and M.T.M. conceived the study. M.G.B. carried out TEM and XRD measurements, analyzed data, and assisted with electrochemistry and materials synthesis. D.Y., M.X., and B.C.M. synthesized materials. S.H., X.S., D.S., and R.R.U. assisted with TEM measurements. B.W. and T.Z. developed and implemented the chemomechanical simulations. M.P. and S.X. performed nanoindentation experiments. J.A.L., N.P.K., and F.J.Q.C. synthesized thin films and performed electrochemical

experiments. M.T.M. guided the project. M.G.B. and M.T.M. wrote the paper with input from all authors.

## DECLARATION OF INTERESTS

The authors declare no competing interests.

Received: January 16, 2018

Revised: May 5, 2018

Accepted: May 25, 2018

Published: June 19, 2018

## REFERENCES

1. Thackeray, M.M., Wolverton, C., and Isaacs, E.D. (2012). Electrical energy storage for transportation—approaching the limits of, and going beyond, lithium-ion batteries. *Energ. Environ. Sci.* 5, 7854–7863.
2. Dunn, B., Kamath, H., and Tarascon, J.-M. (2011). Electrical energy storage for the grid: a battery of choices. *Science* 334, 928–935.
3. Kang, H., Liu, Y., Cao, K., Zhao, Y., Jiao, L., Wang, Y., and Yuan, H. (2015). Update on anode materials for Na-ion batteries. *J. Mater. Chem. A* 3, 17899–17913.
4. Yabuuchi, N., Kubota, K., Dahbi, M., and Komaba, S. (2014). Research development on sodium-ion batteries. *Chem. Rev.* 114, 11636–11682.
5. Chevrier, V.L., and Ceder, G. (2011). Challenges for Na-ion negative electrodes. *J. Electrochem. Soc.* 158, A1011–A1014.
6. Slater, M.D., Kim, D., Lee, E., and Johnson, C.S. (2013). Sodium-ion batteries. *Adv. Funct. Mater.* 23, 947–958.
7. Jian, Z., Luo, W., and Ji, X. (2015). Carbon electrodes for K-ion batteries. *J. Am. Chem. Soc.* 137, 11566–11569.
8. Eftekhari, A., Jian, Z., and Ji, X. (2017). Potassium secondary batteries. *ACS Appl. Mater. Interfaces* 9, 4404–4419.
9. Kundu, D., Talaie, E., Duffort, V., and Nazar, L.F. (2015). The emerging chemistry of sodium ion batteries for electrochemical energy storage. *Angew. Chem. Int. Ed.* 54, 3431–3448.
10. Kim, H., Kim, J.C., Bo, S.-H., Shi, T., Kwon, D.-H., and Ceder, G. (2017). K-ion batteries based on a P2-type  $K_{0.6}CoO_2$  cathode. *Adv. Energy Mater.* 7, 1700098.
11. Boebinger, M.G., Xu, M., Ma, X., Chen, H., Unocic, R.R., and McDowell, M.T. (2017). Distinct nanoscale reaction pathways in a sulfide material for sodium and lithium batteries. *J. Mater. Chem. A* 5, 11701–11709.
12. Pramudita, J.C., Sehrawat, D., Goonetilleke, D., and Sharma, N. (2017). An initial review of the status of electrode materials for potassium-ion batteries. *Adv. Energy Mater.* <https://doi.org/10.1002/aenm.201602911>.
13. Zhao, J., Zou, X., Zhu, Y., Xu, Y., and Wang, C. (2016). Electrochemical intercalation of potassium into graphite. *Adv. Funct. Mater.* 26, 8103–8110.
14. Tian, B., Tang, W., Leng, K., Chen, Z., Tan, S.J.R., Peng, C., Ning, G.-H., Fu, W., Su, C., Zheng, G.W., et al. (2017). Phase transformations in  $TiS_2$  during K intercalation. *ACS Energy Lett.* 2, 1835–1840.
15. Xiao, N., McCulloch, W.D., and Wu, Y. (2017). Reversible dendrite-free potassium plating and stripping electrochemistry for potassium secondary batteries. *J. Am. Chem. Soc.* 139, 9475–9478.
16. Wang, Q., Zhao, X., Ni, C., Tian, H., Li, J., Zhang, Z., Mao, S.X., Wang, J., and Xu, Y. (2017). Reaction and capacity fading mechanisms of tin nanoparticles in potassium-ion batteries. *J. Phys. Chem. C* 121, 12652–12657.
17. Liu, X.H., Zheng, H., Zhong, L., Huang, S., Karki, K., Zhang, L.Q., Liu, Y., Kushima, A., Liang, W.T., Wang, J.W., et al. (2011). Anisotropic swelling and fracture of silicon nanowires during lithiation. *Nano Lett.* 11, 3312–3318.
18. Lee, S.W., McDowell, M.T., Berla, L.A., Nix, W.D., and Cui, Y. (2012). Fracture of crystalline silicon nanopillars during electrochemical lithium insertion. *Proc. Natl. Acad. Sci. USA* 109, 4080–4085.
19. Liu, N., Lu, Z., Zhao, J., McDowell, M.T., Lee, H.W., Zhao, W., and Cui, Y. (2014). A pomegranate-inspired nanoscale design for large-volume-change lithium battery anodes. *Nat. Nanotechnol.* 9, 187–192.
20. McDowell, M.T., Xia, S., and Zhu, T. (2016). The mechanics of large-volume-change transformations in high-capacity battery materials. *Extreme Mech. Lett.* 9, 480–494.
21. McDowell, M.T., Lu, Z., Koski, K.J., Yu, J.H., Zheng, G., and Cui, Y. (2015). In situ observation of divergent phase transformations in individual sulfide nanocrystals. *Nano Lett.* 15, 1264–1271.
22. Li, S., Niu, J., Zhao, Y.C., So, K.P., Wang, C., Wang, C.A., and Li, J. (2015). High-rate aluminum yolk-shell nanoparticle anode for Li-ion battery with long cycle life and ultrahigh capacity. *Nat. Commun.* 6, 7872.
23. Yang, H., Fan, F., Liang, W., Guo, X., Zhu, T., and Zhang, S. (2014). A chemo-mechanical model of lithiation in silicon. *J. Mech. Phys. Solids* 70, 349–361.
24. Zhao, K., Pharr, M., Wan, Q., Wang, W.L., Kaxiras, E., Vlassak, J.J., and Suo, Z. (2012). Concurrent reaction and plasticity during initial lithiation of crystalline silicon in lithium-ion batteries. *J. Electrochem. Soc.* 159, A238–A243.
25. Douglas, A., Carter, R., Oakes, L., Share, K., Cohn, A.P., and Pint, C.L. (2015). Ultrafine iron pyrite ( $FeS_2$ ) nanocrystals improve sodium-sulfur and lithium-sulfur conversion reactions for efficient batteries. *ACS Nano* 9, 11156–11165.
26. Whiteley, J.M., Hafner, S., Han, S.S., Kim, S.C., Oh, K.H., and Lee, S.H. (2016).  $FeS_2$ -imbedded mixed conducting matrix as a solid battery cathode. *Adv. Energy Mater.* 6, 1600495.
27. Shao-Horn, Y., Osmialowski, S., and Horn, Q.C. (2002). Nano- $FeS_2$  for commercial  $Li/FeS_2$  primary batteries. *J. Electrochem. Soc.* 149, A1499–A1502.
28. Yersak, T.A., Macpherson, H.A., Kim, S.C., Le, V.-D., Kang, C.S., Son, S.-B., Kim, Y.-H., Trevey, J.E., Oh, K.H., Stoldt, C., et al. (2013). Solid state enabled reversible four electron storage. *Adv. Energy Mater.* 3, 120–127.
29. Chen, K., Zhang, W., Xue, L., Chen, W., Xiang, X., Wan, M., and Huang, Y. (2017). Mechanism of capacity fade in sodium storage and the strategies of improvement for  $FeS_2$  anode. *ACS Appl. Mater. Interfaces* 9, 1536–1541.
30. Fong, R., Dahn, J.R., and Jones, C.H.W. (1989). Electrochemistry of pyrite-based cathodes for ambient temperature lithium batteries. *J. Electrochem. Soc.* 136, 3206–3210.
31. Zhang, S.S. (2015). The redox mechanism of  $FeS_2$  in non-aqueous electrolytes for lithium and sodium batteries. *J. Mater. Chem. A* 3, 7689–7694.
32. Macpherson, H.A., and Stoldt, C.R. (2012). Iron pyrite nanocubes: size and shape considerations for photovoltaic application. *ACS Nano* 6, 8940–8949.
33. Wang, F., Yu, H.C., Chen, M.H., Wu, L., Pereira, N., Thornton, K., Van der Ven, A., Zhu, Y., Amatucci, G.G., and Graetz, J. (2012). Tracking lithium transport and electrochemical reactions in nanoparticles. *Nat. Commun.* 3, 1201.
34. He, K., Xin, H.L., Zhao, K., Yu, X., Nordlund, D., Weng, T.-C., Li, J., Jiang, Y., Cadigan, C.A., Richards, R.M., et al. (2015). Transitions from near-surface to interior redox upon lithiation in

- conversion electrode materials. *Nano Lett.* 15, 1437–1444.
35. Butala, M.M., Mayo, M., Doan-Nguyen, V.V.T., Lumley, M.A., Göbel, C., Wiaderek, K.M., Borkiewicz, O.J., Chapman, K.W., Chupas, P.J., Balasubramanian, M., et al. (2017). Local structure evolution and modes of charge storage in secondary Li-FeS<sub>2</sub> cells. *Chem. Mater.* 29, 3070–3082.
36. Liu, X.H., Wang, J.W., Huang, S., Fan, F., Huang, X., Liu, Y., Krlyuk, S., Yoo, J., Dayeh, S.A., Davydov, A.V., et al. (2012). In situ atomic-scale imaging of electrochemical lithiation in silicon. *Nat. Nanotechnol.* 7, 749–756.
37. Liu, X.H., Liu, Y., Kushima, A., Zhang, S., Zhu, T., Li, J., and Huang, J.Y. (2012). In situ TEM experiments of electrochemical lithiation and delithiation of individual nanostructures. *Adv. Energy Mater.* 2, 722–741.
38. McDowell, M.T., Ryu, I., Lee, S.W., Wang, C., Nix, W.D., and Cui, Y. (2012). Studying the kinetics of crystalline silicon nanoparticle lithiation with in situ transmission electron microscopy. *Adv. Mater.* 24, 6034–6041.
39. McDowell, M.T., Lee, S.W., Nix, W.D., and Cui, Y. (2013). 25th anniversary article: understanding the lithiation of silicon and other alloying anodes for lithium-ion batteries. *Adv. Mater.* 25, 4966–4985.
40. Mukhopadhyay, A., Kali, R., Badjate, S., Tokranov, A., and Sheldon, B.W. (2014). Plastic deformation associated with phase transformations during lithiation/delithiation of Sn. *Scr. Mater.* 92, 47–50.
41. Xiao, X., Liu, P., Verbrugge, M.W., Haftbaradaran, H., and Gao, H. (2011). Improved cycling stability of silicon thin film electrodes through patterning for high energy density lithium batteries. *J. Power Sources* 196, 1409–1416.
42. Gabrisch, H., Wilcox, J., and Doeff, M.M. (2008). TEM study of fracturing in spherical and plate-like LiFePO<sub>4</sub> particles. *Electrochim. Solid State Lett.* 11, A25–A29.
43. Cortes, F.J.Q., Boebinger, M.G., Xu, M., Ulvestad, A., and McDowell, M.T. (2018). Operando synchrotron measurement of strain evolution in individual alloying anode particles within lithium batteries. *ACS Energy Lett.* 3, 349–355.
44. McDowell, M.T., Lee, S.W., Harris, J.T., Korgel, B.A., Wang, C., Nix, W.D., and Cui, Y. (2013). In situ TEM of two-phase lithiation of amorphous silicon nanospheres. *Nano Lett.* 13, 758–764.
45. Liu, X.H., Zhong, L., Huang, S., Mao, S.X., Zhu, T., and Huang, J.Y. (2012). Size-dependent fracture of silicon nanoparticles during lithiation. *ACS Nano* 6, 1522–1531.
46. Yang, H., Huang, S., Huang, X., Fan, F., Liang, W., Liu, X.H., Chen, L.-Q., Huang, J.Y., Li, J., Zhu, T., et al. (2012). Orientation-dependent interfacial mobility governs the anisotropic swelling in lithiated silicon nanowires. *Nano Lett.* 12, 1953–1958.
47. Epler, E., Roddatis, V.V., and Volkert, C.A. (2016). Measuring mechanical properties during the electrochemical lithiation of silicon. *Energy Technol.* 4, 1575–1581.
48. Pharr, M., Choi, Y.S., Lee, D., Oh, K.H., and Vlassak, J.J. (2016). Measurements of stress and fracture in germanium electrodes of lithium-ion batteries during electrochemical lithiation and delithiation. *J. Power Sources* 304, 164–169.
49. Nadimpalli, S.P.V., Sethuraman, V.A., Bucci, G., Srinivasan, V., Bower, A.F., and Guduru, P.R. (2013). On plastic deformation and fracture in Si films during electrochemical lithiation/delithiation cycling. *J. Electrochem. Soc.* 160, A1885–A1893.
50. Kondekar, N.P., Boebinger, M.G., Woods, E.V., and McDowell, M.T. (2017). In situ XPS investigation of transformations at crystallographically oriented MoS<sub>2</sub> interfaces. *ACS Appl. Mater. Interfaces* 9, 32394–32404.